RESEARCH ARTICLE

On the corrosion behavior and microstructural characterization of Al2024 and Al2024/Ti$_2$SC MAX phase surface composite through friction stir processings

A. Heidarpour[1] · Z. S. Mousavi[1] · S. Karimi[1] · S. M. Hosseini[1]

Abstract

In this paper, aluminum composites reinforced by the Ti$_2$SC MAX phase were fabricated through friction stir processing (FSP). The effects of FSP and the addition of Ti$_2$SC MAX phase on the electrochemical behavior of the surface composite were studied in a 3.5 wt. % NaCl solution. Optical microscopy (OM) and scanning electron microscopy, along with energy-dispersive spectroscopy (SEM–EDS), were employed to investigate the microstructure of the samples. The corrosion behavior of the base metal and FSPed samples with and without Ti$_2$SC-reinforcement particles was examined by different electrochemical methods such as cyclic voltammetry (CV), potentiodynamic polarization, and electrochemical impedance spectroscopy (EIS). Microstructural studies revealed that FSP leads to fine grain structure and reduction in Al$_2$CuMg strengthening precipitates content. The corrosion behavior of Al2024 depends on microstructural characteristics such as grain size, Ti$_2$SC-reinforcement particle size, and distribution of Al$_2$CuMg precipitates. The dissolution of second phase particles (Al$_2$CuMg) present in Al2024 aluminum increases the corrosion resistance of the Al2024 alloy. Also, adding the Ti$_2$SC MAX phase improved the corrosion resistance of the surface composites.

✉ S. Karimi
  s.karimi@hut.ac.ir

[1] Department of Metallurgy and Materials Engineering, Hamedan University of Technology, 65155-579 Hamedan, Iran

Graphic abstract
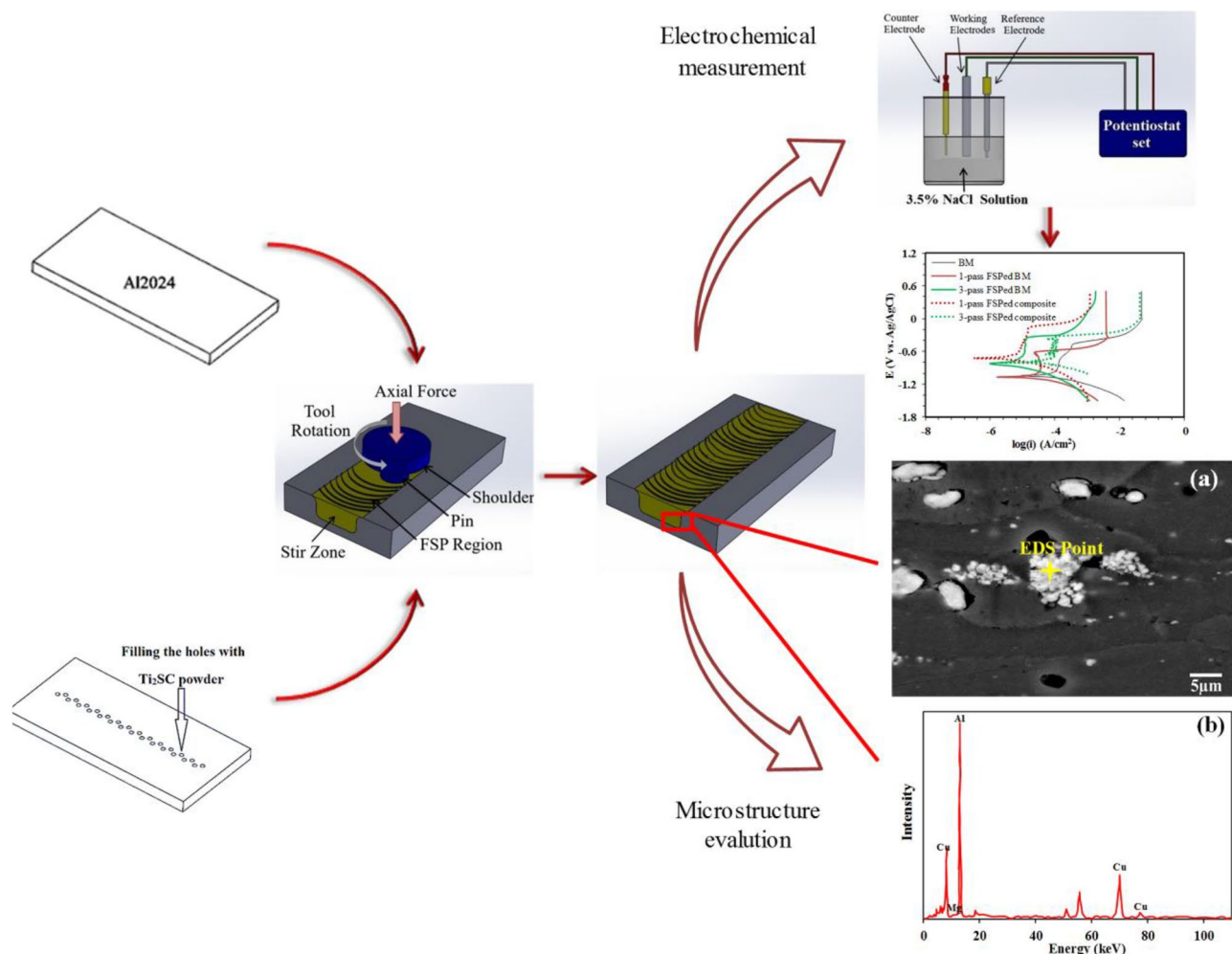
Keywords Friction stir processing · Corrosion behavior · Ti$_2$SC · Electrochemical impedance spectroscopy

1 Introduction

Aluminum and its alloys are frequently employed in various industries, especially in the marine, aerospace, and transportation industries, due to their exclusive properties such as high ductility, high strength-to-weight ratio, and high corrosion resistance [1]. It has been reported that the formation of a thin film of aluminum oxide on its surface leads to an excellent corrosion resistance to various electrolytes [2, 3]. Metal matrix nanocomposites have been widely used in recent years due to their diverse properties and variations in production methods. Using ceramic reinforcing particles in the aluminum matrix improves corrosion resistance, strength, wear resistance, and elastic modulus and declines the coefficient of thermal expansion compared to the matrix material. The material properties of nanocomposites depend

on the amount and distribution of enhancers in the matrix [4]. The advantages of particle-reinforced aluminum (AMC) matrix composites over other types of composites are the ease of fabrication, lower cost, and isotropic properties [5].

The second phase in Al alloys weakens the corrosion resistance by acting as preferential sites for corrosion, especially matrix−reinforcement interface and areas adjoining grain boundaries [6]. Friction stir processing (FSP) represents a process in which a solid-state technique is employed to modify the surface and microstructure of materials. During FSP, the temperature increases due to the severe plastic deformation induced by rotation and friction between the tool and the workpiece [7]. According to Chanakyan and Paidar studies [8, 9], the pass numbers of FSP have a significant impact on the grains refinement and the improvement of microstructure, mechanical properties, and corrosion

behavior [10]. To meet the corrosion challenges, distributing, dissolving, and re-precipitating of the second phase can be applied by the FSP approach. Any changes in particle distribution by FSP could improve corrosion resistance considerably [11].

In recent years, few studies have been conducted to discover the effects of FSP on the corrosion performance of Al alloys. A handful of studies have demonstrated an improvement in corrosion resistance by employing FSP. Soleymani et al. [12] believed that FSP could enhance corrosion resistance. According to Surekha et al. [13] findings, multipass FSP promotes corrosion resistance attributed to the dissolution of $CuAl_2$ particles in the aluminum matrix. Also, Rao et al. [14] reported that FSP causes the better corrosion behavior of Al-30Si alloy due to the formation of a denser and thicker passive layer on the surface.

However, some studies have shown a negative effect of FSP on the corrosion characteristic of aluminum alloys. For instance, it has been reported that the severe plastic deformation by the repeated FSP technique causes fragments and disperses silicon particles in the matrix, leads to increasing the galvanic corrosion [15]. Mazaheri et al. [16] studied the influences of FSP pass numbers on the electrochemical behavior of Al6061. Their studies proclaimed that corrosion resistance of the FSPed samples is considerably lower than that of the base metal.

The MAX phases have unique properties such as thermal conductivity, machinability, high-temperature resistance, high elastic modulus, and oxidation and corrosion resistance [17]. The consequence of FSP pass numbers on the corrosion behavior of the Al2024 matrix and the surface composites by the Ti_2SC MAX phase have not yet been studied and should be investigated in future research. Therefore, the main goal of this research is to predict the electrochemical behavior of base aluminum 2024 alloy and $Al2024/Ti_2SC$ surface composite prepared through FSP. Also, the effect of FSP pass numbers on the distribution and dispersion of Ti_2SC particles was investigated.

2 Experimental methods

The base metal used in this investigation was a commercially available wrought plate of Al2024-T4 with a thickness of 6 mm. The composition of Alloy is given in Table 1.

The FSP machine employed in our experiment was a horizontal-reinforced milling machine. A cylindrical WC pin with a 4 mm length, 5 mm diameter, and 17.5 mm shoulder diameter was used in the experiments. A groove of 1 mm width and 2 mm depth was made in the middle of the workpiece and was then filled with the reinforcement. The groove is placed along the centerline of the tool. The volume of reinforcements depends on the groove size, and since a fixed and identical groove was used for all samples, the overall volume fraction of composites was constant. The theoretical and actual volume fractions of particles were calculated using the following expressions.

Theoretical volume fraction V_t

$$= (\text{Area of groove} / \text{Projected area of tool pin}) \times 100 \tag{1}$$

Actual volume fraction V_a

$$= (\text{Area of groove} / \text{Area of surface composite}) \times 100 \tag{2}$$

$$\text{Area of groove} = \text{Groove width} \times \text{Groove depth} \tag{3}$$

$$\text{The projected area of tool pin} = \text{Pin diameter} \times \text{Pin length} \tag{4}$$

Then the theoretical volume fraction and actual volume fraction of composites were 12 and 8 vol%, respectively. The presence of defects limits the sample performance. In order to fabricate flawless specimens, the FSP process parameters must be optimized. According to the previous report [18], the rotation speed, movement velocity, immersion depth, and tilt angle used in this research were 1000 rpm, 112 mm/min, 3 mm, and 3°, respectively.

For FSP experiments, the appropriate size of Al2024 sheets with a dimension of $100 \times 50 \times 6$ mm^3 size was cut. The surface of the Al2024 plates was polished and cleaned. Then, specimens with and without Ti_2SC particles were subjected to FSP method.

Ti_2SC powders with a mean particle size of 2 μm nm and a standard deviation of less than 180 nm used in this study were synthesized by mechanical alloying which is described in our previous study [19].

To investigate the microstructure of the samples, the surface of samples was grinded using emery paper of 600, 1000, and 2000 grade and polished, then etched with Keller's reagent (1 ml of HF, 1.5 ml of HCl, 2.5 ml of HNO_3 in 95 ml of distilled water). Afterwards, transverse sections were examined by optical microscope, and also surfaces of the samples were investigated by scanning electron microscope (SEM), which were equipped with energy-dispersive X-ray spectroscopy (EDS).

Table 1 Chemical composition of Al2024

Elements	Al	Cu	Mg	Mn	Fe	Si	Zn	Ga
wt.%	92.9	4.89	1.29	0.496	0.290	0.0487	0.0159	0.0152

Electrochemical measurements were carried out with a conventional three-electrode electrochemical cell using a Potentiostat set (Iviumstat compact 20250 H) controlled by Ivium soft electrochemistry software. Measurements were performed in the air atmosphere and room temperature. The samples were used as working electrodes; the counter electrode and the reference electrode were Pt and Ag/AgCl electrodes. All the potentials reported in this research are versus the Ag/AgCl reference electrode.

The test solution was 3.5% NaCl solutions under room temperature at a pH value of 7.5–8.0. Before each electrochemical experiment, the samples' surfaces were polished mechanically using emery SiC papers of 400, 600, and 800 grade. The working electrode was washed with distilled water several times to remove any physically absorbed particles, then it was dried and inserted into the test solution. However, to ensure the reproducibility of the results, each test was performed at least twice. All electrochemical tests (including potentiodynamic polarization, CV, and EIS analysis) were only started after the open circuit potential (OCP) reaching within ± 5 mV. For the potentiodynamic polarization test, the current values were recorded in the range -1.5 to $+0.5$ V vs. Ag/AgCl at a constant scan rate of 1 mV/s and then converted to the current density by figuring the surface area. Cyclic voltammetry (CV) tests were carried out for the Al electrode from negative to positive in the potential range of -1.5 to 0.5 V vs. Ag/AgCl at a constant scan rate of 20 mV/s. Additionally, electrochemical impedance spectra (EIS) experiments were carried out in the frequency range of 10^5 Hz to 0.1 Hz at OCP. The acquisition rate of the amplitude of the perturbation signal was 10 points per decade and 10 mV, respectively.

3 Result and discussion

3.1 Microstructure evaluation

Figure 1 shows a typical micrograph of the cross-section of the base metal and 1-pass FSPed samples. The heating of friction and severe plastic deformation imposed by FSP leads to a significant evolution in the microstructure, which consists of three distinct regions, namely the stir zone (SZ),

the thermomechanically affected zone (TMAZ), and the heat-affected zone (HAZ). It should be noted that HAZ is not visible in this figure due to the high thermal conductivity of aluminum [16].

During the FSP, a sharp rise in temperature and plastic deformation leads to the formation of fine equiaxed grain in the SZ. High temperature can cause the annealing and grain growth within the SZ or lead to the formation of dynamic crystallized grains and a reduction in grain size in the SZ [18]. In addition to dynamic recrystallization, the presence of reinforcement also refines the grain. Reinforcing particles prevent the growth of newly crystallized grains by several mechanisms such as pinning effect [18] or particle dragging [20]. Therefore, in this case, grain refining originating from dynamic recrystallization, annealing, and grain growth are two competitive processes. It can be seen that the grain refinement of Al2024 is applied during the FSP.

The SZ zone is subjected to severe deformation during the FSP, which results in a structure with fine and uniform distribution of precipitates in the microstructure. In all cases, there is a very well bonding between SZ and BM and no defects (i.e., voids or cracks) are visible. Furthermore, modification and refinement of the grain structure occurred in the SZ, which resulted in a decrement of the grain size.

Figure 2 shows the cross-sectional optical micrograph stir zone of FSPed samples with different pass numbers. It can be seen that the FSP led to the high grain refinement for whole samples. In this case, modification and refinement of the grain structure occurred in the SZ, which led to a reduction in grain size in the area. The average grain size of the as-received Al2024 was 50 μm, which decreased to 2 μm after FSP. This phenomenon corresponds to the dynamic recrystallization process [21]. A further reduction in grain size in the SZ was seen (grain size of 1 μm) by adding Ti_2SC particles during FSP. This can be related to two major reasons, including the dynamic recrystallization and the presence of reinforcement precipitate (Ti_2SC) in the base metal (Al2024). These precipitates prevent the new crystallized grains from coarsening during the process.

FSP leads to the friction between the shoulder and workpiece and thermo-mechanical deformation in the FSP zone, increasing the temperature to 0.6–$0.9T_m$, where T_m is the melting temperature of base metal. At high temperatures,

Fig. 1 Optical micrograph of the aluminum 2024: **a** base metal, and **b** the stir zone of 1-pass FSPed sample
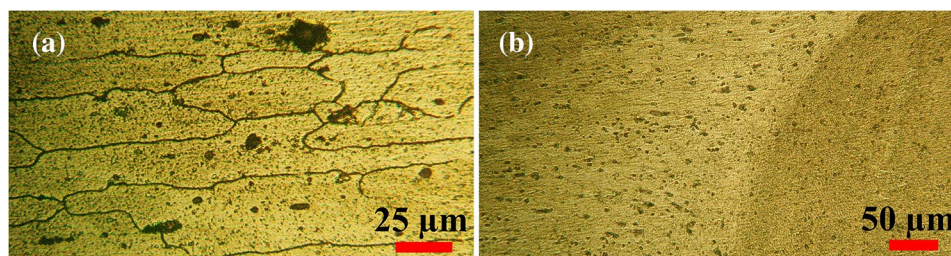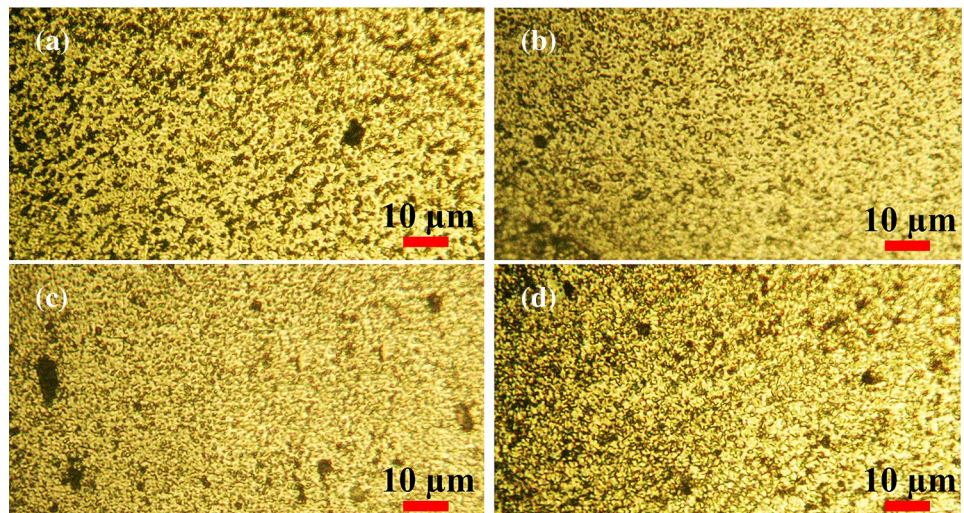
Fig. 2 OM micrographs of stir zone of specimens **a** 1-pass FSPed without Ti_2SC particles, **b** 3-pass FSPed without Ti_2SC particles, **c** 1-pass FSPed with Ti_2SC particles, and **d** 3-pass FSPed with Ti_2SC particles

these precipitates in aluminum alloys could be dissolved or coarsen into Al base metal depending on the maximum temperature reached and the alloy types [22].

To confirm the dissolution of the second phase, SEM images were used. Figure 3 compares the SEM micrograph precipitates of the base metal zone with the in FSPed surface samples. As shown in Fig. 3b and c, several precipitates dissolve in the matrix due to the rising temperature of about 0.6–0.9T_m during FSP. A more refined and uniform distribution of precipitates was created by applying FSP. Table 2 demonstrates the composition of precipitates at different passes by the aid of EDS analyses. Since the precipitates were not visible by optical microscopy, SEM–EDS line scan was carried out to display the dissolution of second phase particles in the FSPed matrix compared to the base metal. Compositional characterization of the particles demonstrates a significant presence of microscale dispersion of Al_2CuMg precipitates (S phase). As it turns out

Fig. 3 SEM micrograph of **a** Al2024 alloy before FSP, **b** after 1-pass FSP, and **c** after 3-pass FSP
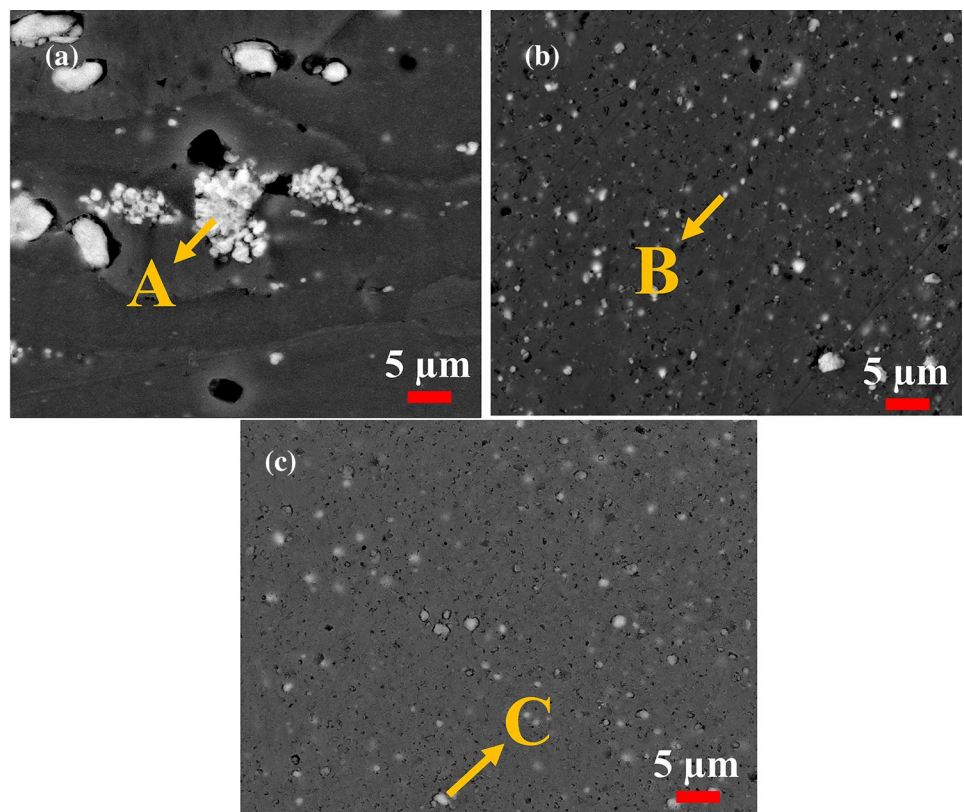
Table 2 EDS analyses of different precipitates highlighted with A, B, and C in FSP and base metal regions are shown on the micrographs of Fig. 3

Location	Element, composition (wt. %)		
	Al	Cu	Mg
A (BM)	44.65	54.58	0.77
B (1-pass FSPed Al2024)	80.47	16.73	2.80
C (3-pass FSPed Al2024)	83.69	14.22	2.09

Fig. 5 Open circuit potential vs. time for all studied samples measured in 3.5 wt% NaCl solution at 25 °C

from Fig. 3 and Table 2, the FSP causes a significant variation in the chemical composition of the second phase. It is clear that Mg in the S phase increases, and on the other side, the concentration of copper in the S phase decreases by the FSP method. Accordingly, the aluminum content of precipitates sharply enhanced from 44.65% to the range of 80.47−83.69%. On the other hand, the FSP method promotes the homogeneous composition of Al2024 and resulting in Cu-poor precipitates.

Figure 4 shows the SEM–EDS line scan results of FSPed samples, base metal, and the copper concentration variation at different passes. It is interpreted through the analysis of copper that the fraction of the second phase has become higher as the number of FSP passes increases, indicating
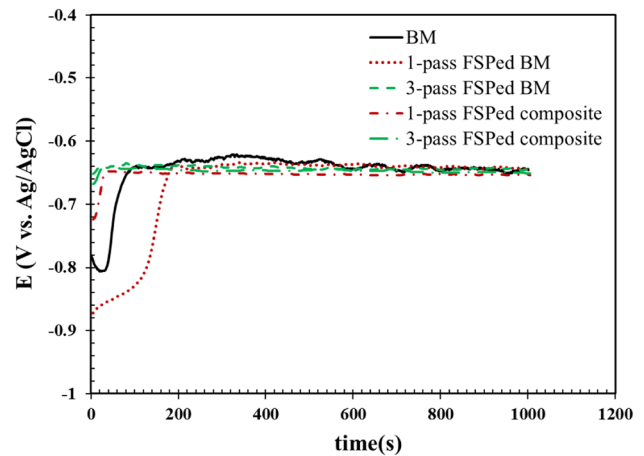
the rearrangement of copper into the aluminum matrix in the FSPed samples in comparison with the base metal. It can be seen that the Cu concentration of particles in the base metal is lower than FSPed samples even after a single pass. A significant increase in copper concentration is observed in the 3-pass FSPed sample, which can be attributed to the higher heat input in the 3-pass FSPed sample than the 1-pass sample [23].

Fig. 4 SEM micrographs of **a** BM, **b** 1-pass FSPed Al2024, **c** 3-pass FSPed Al2024, and **d** corresponding EDS line scan analysis spectrum
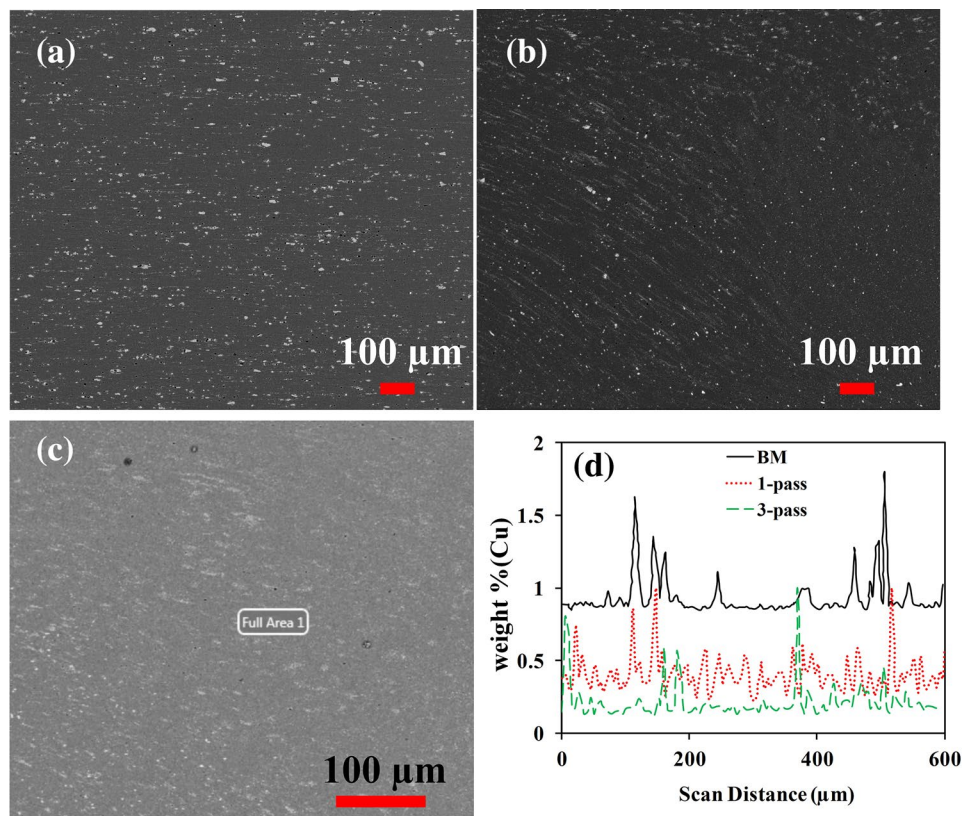
3.2 Corrosion studies

3.2.1 Open circuit potential

To ensure the reproducibility of all the corrosion tests, the working electrode was allowed to reach the OCP. The OCP magnitude for samples can be precisely a sign of their electrochemical activity [24]. The OCP evolution of the base metal and all of the FSPed samples with and without Ti_2SC powders in 3.5% NaCl solution is shown in Fig. 5. The OCP curves of the samples show a similar trend that consists of two steps. At the first stage (0–200 s), OCP values increased significantly, inferring that passivation of surface happened as a consequence of a hydrous aluminum oxides formation on the Al2024 surface in contact with the solution. Then, the curve reaches a steady state, and the OCP remains constant, indicating a dynamic equilibrium is established between the dissolution and formation of hydrous aluminum oxide [25].

The OCP values for all the samples are -0.64 V vs. Ag/AgCl. The time to reach an OCP for 1-pass FSPed Al2024 is longer than that is required for other samples. Increasing the number of passes leads to reduce the pores of the surface and homogenize the microstructure. This can improve the formation of a homogenous and completely sticky passive layer [26]. Figure 5 shows that increasing the pass numbers reduces the equilibrium time at the level of FSPed samples.

3.2.2 Potentiodynamic polarization study

Figure 6 shows the potentiodynamic polarization diagrams of the base metal and FSPed samples in a 3.5% NaCl solution. It is illustrated that all samples (BM, FSPed with and without Ti_2SC) demonstrate the same shapes, in the
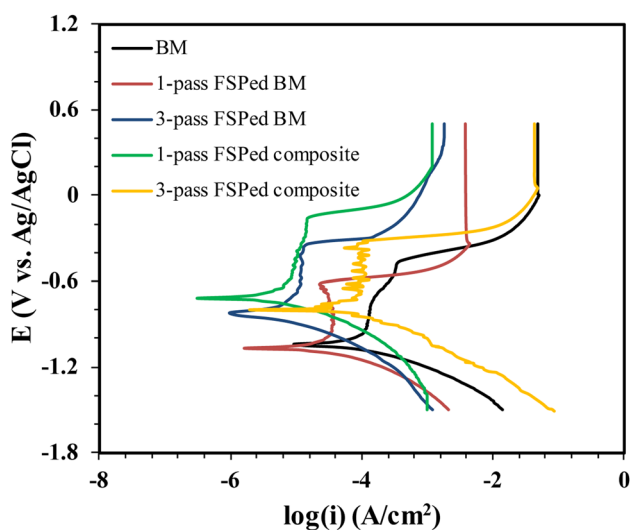

Fig. 6 Potentiodynamic polarization diagrams of the base metal and FSPed samples in a 3.5% NaCl solution

Table 3 The corrosion parameters obtained from the potentiodynamic polarization test of BM and FSPed samples

Sample	$E_{corr.}$ (V vs. Ag/AgCl)	i_p ($\mu A.cm^{-2}$)
BM	-1.00	15.84
1-pass FSPed Al2024	-1.05	79.04
3-pass FSPed Al2024	-0.82	3.62
1-pass FSPed composite	-0.70	2.51
3-pass FSPed composite	-0.75	12.59

cathodic branch, the current reaches gradually to the corrosion potential, and in the anodic branch, directly enters the passive region by increasing the applied potential. On the other hand, there is no active–passive transition in the anodic region, except for the BM. Khatami et al. [27] reported the same passivation behavior for Al2024-T3 alloy, which undergoes the accumulative roll bonding (ARB) process. Moreover, the electrochemical parameters obtained from Fig. 6 are also given in Table 3. The corrosion potential (E_{corr}) and passivation current density (i_p) of Al2024 base metal are -1.00 V vs. Ag/AgCl and 15.84 $\mu A.cm^{-2}$, respectively. The values of corrosion potential of all FSPed samples except 1-pass surface composite (with or without reinforcement-Ti_2SC) are higher than that of the base metal. In contrast, the samples show lower passivation current density. In other words, the E_{corr} of the FSPed samples has been shifted to higher values, and their current density shows lower values. The passivation current density directly correlates with the corrosion rate [13]. The i_p value of the 1-pass and 3-pass FSPed Al2024 samples decreased from 79.04 to 3.62 $\mu A.cm^{-2}$, while i_p value for 1-pass and 3-pass FSPed composite samples increased from 2.51 to 12.59 $\mu A.cm^{-2}$, respectively. Similar results have been reported in recent studies that the increase in the passivation current density is due to an increase in the pass numbers of FSP [14].

Based on the obtained results, the E_{corr} of all FSPed samples increased by increasing the FSP passes from 1 to 3, while the E_{corr} value of FSPed composite samples decreased by the number of FSP passes which increased from 1 to 3. Accordingly, the more positive corrosion potential, the more passively behaves [14]. This finding means that the corrosion resistance of all FSPed samples (with or without reinforcement-Ti_2SC), except 1-pass FSPed Al2024, is more than that of the base metal. Also, it can be derived that the electrochemical resistance of all FSPed samples (with and without Ti_2SC powders) increased significantly with an increment in the number of FSP passes.

As mentioned, all of the FSPed specimens (except 1-pass FSPed Al2024) exhibited a low corrosion rate. Therefore, it can be expressed that FSP leads to the improvement of

the corrosion resistance of Al2024, and some studies have shown an improvement in corrosion behavior by FSP.

As mentioned earlier, the presence of the second phase with the composition of Al_2CuMg (S phase) in the Al2024 matrix was confirmed by using SEM–EDS analysis (see Fig. 3 and Table 2). It is well established that the S phase acts as anodic behavior due to its negative potential. Conversely, the aluminum alloy is a cathode, and a galvanic pair between two phases' S precipitates and the aluminum matrix is generated [28]. It has been reported that pitting corrosion arises on the S precipitates. As pitting corrosion proceeds, dealloying of Mg in S phase occurred, resulting in copper-rich precipitates. Thereby, the S phase acts as a cathode in a galvanic couple between precipitates and substrate due to the positive potential [29].

As can be seen in Table 2, the FSP method encourages the formation of higher Mg content in S phase precipitates. Generally, it can be concluded that FSP reduced the pitting corrosion of Al2024 substrate and retarded the corrosion of the substrate. In addition to pitting corrosion between the S phase and the surrounding matrix, a preferential depletion of copper around the coarse S phase occurred. So, the Cu-depleted matrix surrounding the precipitates has anodic behavior compared to the S phase and the rest of substrate. Based on these results, the localized corrosion of the surrounding the S phase weakened by applying the FSP method.

There are several possible explanations for these findings:

(1) During FSP, near the surface of the metal exposed to local plastic deformation, mixing, and significant friction heating creates a very fine and equiaxed grain microstructure due to dynamic recrystallization in the SZ [30]. In other words, during FSP, the grain refining takes place in the surface layer [26]. Undoubtedly, the existence of a fine-grained structure leads to a high grain boundary density since the grain boundaries are notably higher energy regions than grains. As a result, the corrosion potential 1-pass FSPed sample becomes more negative than the base metal, thereby reducing the corrosion resistance. So, the lower corrosion resistance of the 1-pass FSPed sample compared to base metal is predictable [31]. It is clear that FSP causes the residual stress, and according to the Nernst equation, samples with residual stresses have higher Gibbs free energy and less electrical potential than non-stress samples [32]. As a result, it seems reasonable that 1-pass FSPed samples are likely to have lower corrosion resistance than BM.

(2) The increment in corrosion resistance can be attributed to the rearrangement of the second phase particles in the FSPed samples [23]. Thermomechanical stresses caused by severe plastic deformation through the FSP can break the matrix's precipitates to finer sizes and more homogeneous distribution [33]. Studies have shown that grain size is smaller in FSP areas and precipitates are released, and even in the regions of HAZ and TMAZ, the density of precipitates is lower than in the base materials [22]. Also, an increment in the number of FSP passes causes a reduction in the pores and homogenization of the microstructure. This improves the formation of a homogenous and fully adhering passive layer [26]. The homogeneous microstructure reduces the dissolution and destruction of precipitates and the concentration of precipitates in FSP areas [22]. Accordingly, the dissolving of the precipitates reduces the sites for galvanic corrosion at the FSPed surface [13].

(3) Also, the presence of reinforcing particles affects the electrochemical behavior. While the one-pass reinforced composite sample presented a minimum corrosion rate, the one-pass without Ti_2SC MAX phase particle specimen revealed a poor corrosion performance compared with the one-pass reinforced composite. After 1-pass FSP, the corrosion potential value of the FSPed Al2024 sample decreased from -1.00 to -1.05 V vs. Ag/AgCl, and passivation current density increased from 15.84 to 79.04 $\mu A.cm^{-2}$, respectively. When reinforcing particles were added to base metal during FSP it causes a 0.05 V decrease in corrosion potential and 6.3 times increase in passivation current density of the FSPed composite sample than FSPed Al2024. It can be concluded that adding Ti_2SC particles and performing 1-pass FSP causes the corrosion improvement of Al2024. Additionally, increasing the FSP pass number from one to three passes reduces corrosion resistance due to the formation of high-angle grain boundaries and a high density of dislocation. Increasing the FSP pass number varies the nature of grain boundaries from low to high angle. Increasing the number of low coordinated lattice points behind the passive layer diminishes the passive layer stability [34]. Also, with the increasing number of FPS passes, the penetration depth of the reinforcing particles increases, and the number of particles at the composite level decreases [26]. The density of the reinforcing particles decreases at a certain depth with the increasing pass number, which increases the corrosion rate. Therefore, the increase in passivation current density of samples containing Ti_2SC particles can be justified by increasing the pass number.

3.2.3 Cyclic voltammetry measurements

Figure 7 shows the cyclic polarization curves for all samples in a 3.5% NaCl solution. The polarization curve of these

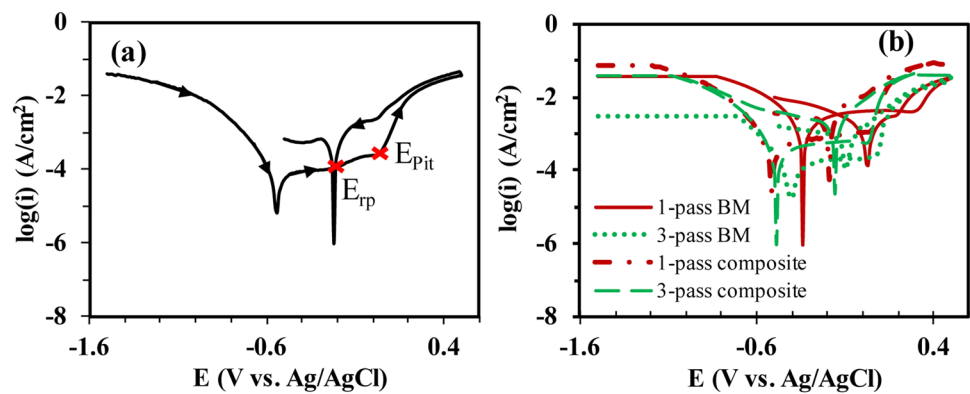**Fig. 7** Cyclic voltammetry curves of **a** base metal and **b** FSPed samples

Table 4 The corrosion parameters of BM and FSPed samples (V vs. Ag/AgCl)

Sample	E_{pit}	E_{rp}	$E_{pit}-E_{rp}$
BM	0.02	−0.21	0.23
1-pass FSPed Al2024	0.35	0.20	0.15
3-pass FSPed Al2024	0.06	−0.07	0.13
1-pass FSPed composite	0.05	−0.17	0.22
3-pass FSPed composite	0.00	−0.14	0.14

samples showed one breakdown potential. The breakdown potential corresponded to the pitting of the grain bodies or intergranular corrosion (IGC). Breakdown potential (E_{pit}) is a measure of pitting onset; thus, materials with more positive breakdown potential indicated better pitting resistance. It has been confirmed that the higher the value of E_{pit}, the more difficult the pitting corrosion [35].

The values of pitting potentials (E_{pit}) and repassivation potentials (E_{rp}) are presented in Table 4. The breakdown potential (E_{pit}) values of all FSPed samples (with or without reinforcement-Ti$_2$SC particles) except 3-pass composite are higher than that of the base metal. This means that the resistance of the pitting corrosion of FSPed samples, except 3-pass composite, is also more than that of the base metal.

According to Table 4, the E_{pit} value of 3-pass FSPed Al2024 is less than 1-pass FSPed Al2024. Moreover, the E_{pit} value of 1-pass FSPed composite samples and 3-pass FSPed composite decreases from 0.05 to 0.00 V vs. Ag/AgCl. It is easy to get that increasing the number of FSP passes leads to an increase in the tendency of FSPed samples to pitting corrosion.

Localized corrosion (pitting corrosion) is the main reason for Al-Cu alloy failure in corrosion environments, including alkaline media [36]. Al$_2$CuMg (S phase) is the most predominant type of intermetallic particle in Al2024 alloy [37]. During FSP, the considerable heat is entered into the sample. This temperature is adequately high to dissolve the second phase into the matrix and increasing the copper content in

the Al matrix during FSP. Since the Al$_2$CuMg phase has an anodic nature compared to the Al matrix, the propagation of copper solubility in the aluminum matrix leads to an increase in the potential difference between the two phases, which raises the driving force for the initiation of pitting corrosion [38]. As the number of passes increases, more particles are dissolved in the aluminum matrix, and the amount of copper in the aluminum matrix has been increased. Therefore, pitting corrosion resistance has been found to decrease with increasing the number of passes attributed to the dissolution of precipitation.

Also, Liu et al. [38] reported similar results in the electrochemical behavior of Al alloy. They have shown that the solubility of copper in the Al matrix was found to be a major point in the initiation of pitting corrosion in aluminum alloys. Repassivation potential is a potential at which the growth rate of pits stops. The amount of hysteresis or the difference between E_{pit}–E_{rp} indicates the amount of localized corrosion [39]. In general, the larger hysteresis loop ($E_{pit} - E_{rp}$) leads to a more significant amount of localized corrosion.

The (E_{pit}-E_{rp}) value of all FSPed samples is less than the base metal, so it can be said that the amount of localized corrosion and the susceptibility of the material to the pit corrosion of all FSPed samples is lower than that of the base metal. Furthermore, the ($E_{pit} - E_{rp}$) value of the 3-pass FSPed Al2024 is more minor than the 1-pass FSPed Al2024. Moreover, the ($E_{pit} - E_{rp}$) value of 3-pass FSPed composite is less than 1-pass FSPed composite. Therefore, it can be said that the amount of localized corrosion of 3-pass FSPed samples is less than 1-pass FSPed samples. These results are attributed to the grain sizes and the density of precipitate particles obtained by FSP. It has been reported that the grain size is an important aspect of the passivation of Al alloys and the rapid formation of a stable passive layer on the metal's surface [40]. As mentioned before, increasing the number of FSP passes causes grain refinement and dissolution of the precipitates and reduces their size. Therefore, a gradual decrease in localized corrosion was observed with the

Fig. 8 EIS results of all of the samples (BM and FSPed samples) in NaCl solution: **a** Nyquist plots; **b** Bode plots
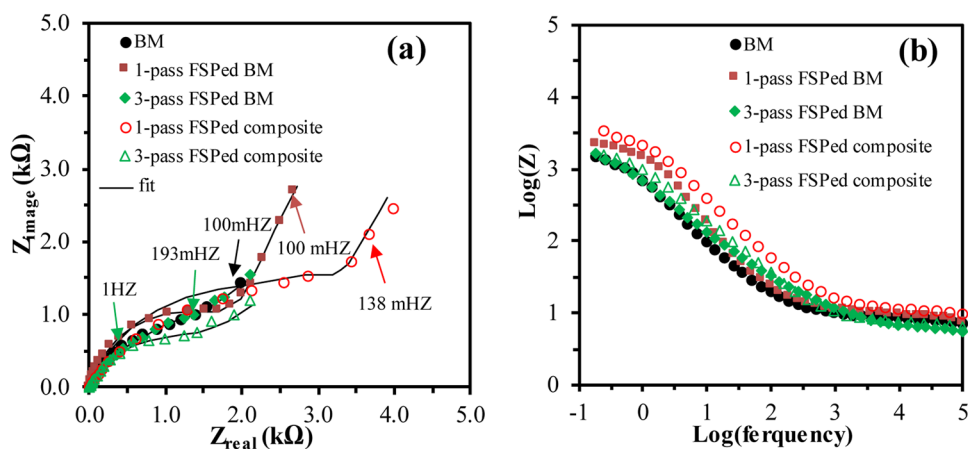
number of FSP passes increasing. Thus, the lower amount of localized corrosion of the specimens with an increasing pass number can be attributed to the considerable reduction of the grain size and the formation of the passive layer on 3-pass FSPed samples.

3.2.4 Electrochemical impedance measurement (EIS)

To further investigate the electrochemical reaction on the surface of samples, electrochemical impedance spectroscopy (EIS) in 3.5 wt% NaCl at open circuit potentials (OCPs) was performed. Figure 8 depicts the measured and calculated Nyquist impedance spectra and Bode plots for the BM and FSPed samples. Generally, the Nyquist impedance spectra in Fig. 8 show two time constants with two electrochemical processes. Additionally, all the experimental Nyquist diagrams showed a depressed semi-circular shape with the center under the real impedance axis. This behavior is not unusual in metal electrodes [41].

The first depressed circle is related to the diffusion process through passive films on the surface. It has been previously reported that the low-frequency semi-circle is attributed to diffusion-controlled processes and transport phenomena in oxidized products [41]. Hence, it can be concluded that aluminum electrochemical behavior at OCP contains both charge transfer and diffusion processes. The second semi-circle at a lower frequency is a capacitive semi-circle usually related to double-layer capacitance, including a charge transfer resistance in the electrolyte interface (NaCl solution) and electrode surface (aluminum oxidized). It has been reported that when the alloys and alloy-based coatings of aluminum are immersed in the NaCl solution, a thin layer of oxide forms on the surface [42]. The cathodic and anodic reactions occurring during Al alloy corrosion in 3.5 wt% NaCl are reduction of oxygen and Al dissolution or oxidation according to the following reactions [43]:
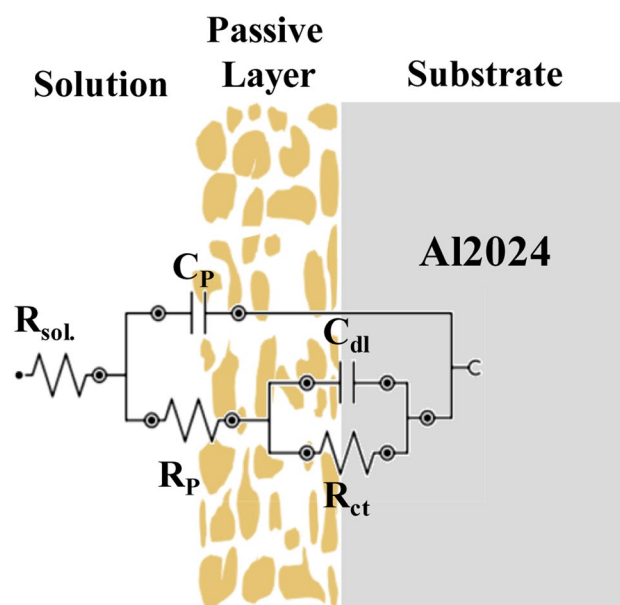

Fig. 9 Schematic of an equivalent circuit on the porous electrode interface

$$O_2 + 2H_2O + 4e^- \rightarrow 4OH^- \tag{5}$$

$$Al \rightarrow Al^{3+} + 3e^- \tag{6}$$

$$2Al + 6OH^- \rightarrow Al_2O_3 + 3H_2O + 6e^- \tag{7}$$

A schematic of an equivalent circuit on the porous electrode interface is depicted in Fig. 9. The electrical parameters of the equivalent electrical circuit are given in Table 5. The circuit consists of a solution resistance (R_s) and two parallel capacitance loops, R_p/C_p and R_{ct}/C_{dl}, over the whole frequency range. The inner circuit (second loop) relates to the interface of aluminum and solution, which consists of the combination of the capacitance of double layer (C_{dl}) and

Table 5 Values of the equivalent circuit parameters of Fig. 9

Sample	R_s ($\Omega.cm^2$)	R_p ($\Omega.cm^2$)	C_p ($\mu F.cm^{-2}$)	R_{ct} ($\Omega.cm^2$)	C_{dl} ($\mu F.cm^{-2}$)
BM	8.61	7575.4	0.94	2028	0.79
1-pass FSPed Al2024	10.30	1516.2	0.95	2755	0.86
3-pass FSPed Al2024	7.41	1359.8	1.46	4859	0.66
1-pass FSPed composite	5.66	5961.0	0.79	5090	0.79
3-pass FSPed composite	6.79	2242.0	0.97	2142	0.74

charge transfer resistance (R_{ct}). The outer circuit is related to the properties of the porous passive layer formed on Al, with passive capacitance (C_p) and charge transfer resistance of the passive film (R_p).

The values of R_{sol} are in the range of 5.66–10.30 $\Omega.cm^{-2}$, which is approximately low for all samples. R_{ct} is the charge transfer resistance, which indicates the corrosion rate of the sample. The higher the R_{ct}, the lower the corrosion rate [44]. In other words, increasing the R_{ct} value indicates a decrease in the dissolution rate of the metal after immersion in the neutral salt solution. Furthermore, the increase in R_{ct} indicates a higher resistance to active dissolution [45]. As shown in Table 4, the R_{ct} value of Al2024 base metal is 2028 $\Omega.cm^2$. Particularly, for the FSPed sample without powders, the R_{ct} value of the 1-pass increased to 2755 $\Omega.cm^2$, and as the FSP pass was increased to 3-pass, it became higher and reached 4859 $\Omega.cm^2$. The increment in the charge transfer resistance value for 1-pass and 3-pass FSPed samples is fairly correlated with potentiodynamic polarization results. When it comes to corrosion resistance, it was expected that FSPed samples are much more stable than BM (Al2024).

On the other hand, the FSPed samples exhibit higher electrochemical corrosion resistance than the base material, indicating better corrosion protection for FSPed samples. It has been generally believed that the corrosion attitude of aluminum alloys is mostly attributed to the second phase precipitates, which can lead to the favored dissolution of the surrounding Al matrix and therefore results in localized corrosion (pitting corrosion) [45, 46]. In the case of Al2024, it has been reported that Al_2CuMg particles can lead to promoting pitting corrosion [47]. The different contents of the second phase and the impurity elements lead to differences in corrosion resistance [25]. Thus, the higher content of the second phase leads to the poor corrosion resistance of the aluminum alloys. It has been proposed that the dispersion of the Al_2CuMg particles will be more uniform with an increasing number of FSP [47]. In addition to the mentioned argument, the low values of R_{ct} of base metal compared with the FSP samples can be related to the local galvanic cells between the copper-rich precipitates (cathode) and the Al matrix (anode), which enhanced the dissolution of Al [43]. As mentioned earlier, FSP causes the dissolution of precipitates, and the concentration of precipitates in FSP areas is less than that of the base materials. Accordingly, the dissolution of the precipitates declines the points for galvanic coupling, and as a result of this phenomena, local and galvanic corrosion at the composite surface is diminished.

The R_{ct} value of 1-pass FSPed Al2024 is 2755 $\Omega.cm^2$, and for the FSPed sample with Ti_2SC particles, the R_{ct} value increased to 5090 $\Omega.cm^2$. It can be concluded that the addition of Ti_2SC MAX phase particles and performing one-pass FSP improved the corrosion resistance of Al2024. The increment in the charge transfer resistance value for 1-pass FSPed composite samples is confirmed by potentiodynamic polarization results. Further grain refinement and reduction of casting defects by filling the cavities after the addition of reinforcing particles are the reasons for improving the corrosion behavior [34].

Table 5 showed that the electrochemical resistance of FSPed composite decreased from 5090 to 2142 $\Omega.cm^2$, increasing the number of passes from 1 to 3. Since with the increasing number of passes, the penetration depth of the reinforcing particles increases, and the number of particles at the composite level decreases, the dislocation density and the high-angle grain boundary increase, so with the increasing number of passes, the corrosion resistance of the alloy decreased. The reduction in the charge transfer resistance value for 1-pass and 3-pass FSPed samples is reasonably correlated with potentiodynamic polarization results. As shown in Table 3, the i_p of FSPed composite samples increases drastically from 2.51 for BM to 12.59 $\mu A.cm^{-2}$ by increasing the number of passes from 1 to 3. Besides, the presence of reinforcing particles and the number of passes affect the electrochemical behavior. While the one-pass FSPed composite sample demonstrated a low corrosion rate, the one-pass FSPed Al2024 sample (without reinforcement particles) demonstrated a poor corrosion resistance and a high rate of corrosion rate compared to the reinforced sample.

The high-frequency impedance shows the corrosion process of the passive layer. The R_p is the resistance of corrosion products on the pit site and oxide film, and its value is measured by the resistance on the pit site [45]. Additionally, the diameter of the semi-circle is attributed to the resistance of the passive layer (R_p). The stability of the passive layer has been increased by an increment in the R_p, which corresponds to the thickening or compactness of the passive layer [27]. As mentioned in Table 4, an increment in FSP number passes, the resistance to pitting corrosion of FSPed Al2024 samples reduced from 0.35 to 0.06 V vs. Ag/AgCl,

and FSPed composite samples decreased from 0.05 to 0 V vs. Ag/AgCl, indicating the value of R_p decreases with an increasing number of passes. So, it is obvious that at the same immersion time, the corroded area on the surface of the 3-FSPed transition specimens is larger than the surface of the 3-FSPed transition specimens.

According to Eq. (8), passive layer capacitance is conversely attributed to the thickness of the passive layer, which serves as a barrier layer from corrosion.

$$C_p = \frac{\varepsilon \varepsilon_0 A}{d_p}, \tag{8}$$

where d_p is the thickness of the electrical passive layer, ε_0 is vacuum permittivity, ε represents a dielectric constant of the passive layer (for Al2024 is equal to 10 [48]), and A is the working electrode area in the electrolyte. The 1-pass FSPed composite sample demonstrates the minimum value of passive layer capacitance (0.79 μF.cm^{-2}), which reflects a maximum thickness of the passive layer. The passive layer on the sample's surface acts as an anti-corrosion barrier, thus enhances the protecting surface from corrosion. These findings confirm the data obtained in potentiodynamic polarization analysis, in which lower current density led to higher protection efficiency.

4 Conclusion

The microstructure and corrosion performance of the Al2024 aluminum alloy and its surface composite reinforced with the Ti_2SC MAX phase have been investigated. The main results could be concluded as follows:

(1) Microstructural surveys indicated that FSP leads to significant grain refinement. Addition of Ti_2SC particles and also increasing pass number made this refinement intensifying.

(2) Based on the potentiodynamic polarization findings, the E_{corr} of the FSPed samples is shifted to higher values, implying that the corrosion behavior of all FSPed samples, except 1-pass FSPed Al2024, showed an improvement compared with the base metal. The result indicated that corrosion resistance of all FSPed samples increased significantly with an increment in FSP passes.

(3) Based on the electrochemical results, the E_{corr} value of FSPed BM samples increased by increasing the number of FSP passes from 1 to 3. It can be expressed that increasing the number of FSP passes leads to improving the corrosion resistance of FSPed Al2024. In contrast, it demonstrated that increasing the number of

FSP passes negatively affects the corrosion behavior of FSPed Al2024 surface composites.

(4) The cyclic voltammetry clearly showed that the pitting corrosion resistance of FSPed samples, except 3-pass composite, is also more than that of the base metal. Also, the susceptibility of the FSPed samples to pitting corrosion was increased by increasing the number of FSP passes.

(5) EIS measurements showed that the FSPed samples exhibit higher electrochemical corrosion resistance. By increasing the number of passes, the corrosion resistance of the FSPed BM samples improves. In contrast, the electrochemical resistance of FSPed composite samples decreased with an increase in the number of passes. The addition of Ti_2SC particles in the structure has caused an increase in the corrosion resistance of 1-pass FSP Al2024.

References

1. Polmear I, St John D, Nie J-F, Qian M (2017) Light alloys: metallurgy of the light metals, 5th edn. Elsevier Inc., Amsterdam
2. Melchers RE (2015) Time dependent development of aluminium pitting corrosion. Adv Mater Sci Eng 2015:1–10. https://doi.org/10.1155/2015/215712
3. Revie RW (2011) Uhlig's corrosion handbook, 3rd edn. Wiley, New Jersey
4. Koli DK, Agnihotri G, Purohit R (2014) A review on properties, behaviour and processing methods for Al-Nano Al_2O_3 composites. Procedia Mater Sci 6:567–589. https://doi.org/10.1016/j.mspro.2014.07.072
5. Kumar S, Reddy SK, Joshi SV (2017) Microstructure and performance of cold sprayed Al-SiC composite coatings with high fraction of particulates. Surf Coatings Technol 318:62–71. https://doi.org/10.1016/j.surfcoat.2016.11.047
6. Ramgopal T, Gouma PI, Frankel GS (2002) Role of grain-boundary precipitates and solute-depleted zone on the intergranular corrosion of aluminum alloy 7150. Corrosion 58:687–697. https://doi.org/10.5006/1.3287699
7. Ma ZY (2008) Friction stir processing technology: a review. Metall Mater Trans A Phys Metall Mater Sci 39(3):642–658. https://doi.org/10.1007/s11661-007-9459-0
8. Chanakyan C, Sivasankar S, Meignanamoorthy M et al (2020) Friction stir processing (FSP) of numerical study based on design of experiment-review. Mater Today Proc 27:748–751. https://doi.org/10.1016/j.matpr.2019.12.035
9. Paidar M, Ojo OO, Ezatpour HR, Heidarzadeh A (2019) Influence of multi-pass FSP on the microstructure, mechanical properties and tribological characterization of Al/B_4C composite fabricated by accumulative roll bonding (ARB). Surf Coatings Technol 361:159–169. https://doi.org/10.1016/j.surfcoat.2019.01.043
10. Moustafa E (2017) Effect of multi-pass friction stir processing on mechanical properties for AA2024/Al_2O_3 nanocomposites. Materials (Basel) 10:1053. https://doi.org/10.3390/ma10091053
11. Sharma R, Singh AK, Arora A et al (2019) Effect of friction stir processing on corrosion of Al-TiB_2 based composite in 3.5 wt.% sodium chloride solution. Trans Nonferrous Met Soc China 29:1383–1392. https://doi.org/10.1016/S1003-6326(19)65045-4

12. Soleymani S, Abdollah-zadeh A, Alidokht SA (2012) Microstructural and tribological properties of Al5083 based surface hybrid composite produced by friction stir processing. Wear 278–279:41–47. https://doi.org/10.1016/j.wear.2012.01.009

13. Surekha K, Murty BS, Rao KP (2008) Microstructural characterization and corrosion behavior of multipass friction stir processed AA2219 aluminium alloy. Surf Coatings Technol 202:4057–4068. https://doi.org/10.1016/j.surfcoat.2008.02.001

14. Rao AG, Katkar VA, Gunasekaran G et al (2014) Effect of multipass friction stir processing on corrosion resistance of hypereutectic Al-30Si alloy. Corros Sci 83:198–208. https://doi.org/10.1016/j.corsci.2014.02.013

15. Salehi M, Saadatmand M, Aghazadeh Mohandesi J (2012) Optimization of process parameters for producing AA6061/SiC nanocomposites by friction stir processing. Trans Nonferrous Met Soc China 22:1055–1063. https://doi.org/10.1016/S1003-6326(11)61283-1

16. Mazaheri Y, Heidarpour A, Jalilvand MM, Roknian M (2019) Effect of friction stir processing on the microhardness, wear and corrosion behavior of Al6061 and Al6061/SiO2 nanocomposites. J Mater Eng Perform 28:4826–4837. https://doi.org/10.1007/s11665-019-04260-3

17. Sun ZM (2011) Progress in research and development on MAX phases: a family of layered ternary compounds. Int Mater Rev 56:143–166. https://doi.org/10.1179/1743280410Y.0000000001

18. Manochehrian A, Heidarpour A, Mazaheri Y, Ghasemi S (2019) On the surface reinforcing of A356 aluminum alloy by nanolayered Ti$_3$AlC$_2$ MAX phase via friction stir processing. Surf Coatings Technol 377:124884. https://doi.org/10.1016/j.surfcoat.2019.08.013

19. Hosseini SM, Heidarpour A, Ghasemi S (2020) Effects of ball milling sequences on the in-situ reactive synthesis of the Ti$_2$SC MAX phase. Adv Appl Ceram 119:204–211. https://doi.org/10.1080/17436753.2020.1732637

20. Hodder KJ, Izadi H, McDonald AG, Gerlich AP (2012) Fabrication of aluminum-alumina metal matrix composites via cold gas dynamic spraying at low pressure followed by friction stir processing. Mater Sci Eng A 556:114–121. https://doi.org/10.1016/j.msea.2012.06.066

21. Ghanbari D, Kasiri Asgarani M, Amini K, Gharavi F (2017) Influence of heat treatment on mechanical properties and microstructure of the Al2024/SiC composite produced by multi–pass friction stir processing. Meas J Int Meas Confed 104:151–158. https://doi.org/10.1016/j.measurement.2017.03.024

22. Abdi behnagh R, Besharati Givi MK, Akbari M (2012) Mechanical properties, corrosion resistance, and microstructural changes during friction stir processing of 5083 aluminum rolled plates. Mater Manuf Process 27:636–640. https://doi.org/10.1080/10426914.2011.593243

23. Surekha K, Murty BS, Prasad Rao K (2011) Comparison of corrosion behaviour of friction stir processed and laser melted AA 2219 aluminium alloy. Mater Des 32:4502–4508. https://doi.org/10.1016/j.matdes.2011.03.033

24. Karimi S, Ghahreman A, Rashchi F (2018) Kinetics of Fe(III)-Fe(II) redox half-reactions on sphalerite surface. Electrochim Acta 281:624–637. https://doi.org/10.1016/j.electacta.2018.05.132

25. Wei YK, Luo XT, Ge Y et al (2019) Deposition of fully dense Al-based coatings via in-situ micro-forging assisted cold spray for excellent corrosion protection of AZ31B magnesium alloy. J Alloys Compd 806:1116–1126. https://doi.org/10.1016/j.jallcom.2019.07.279

26. Rahsepar M, Jarahimoghadam H (2016) The influence of multipass friction stir processing on the corrosion behavior and mechanical properties of zircon-reinforced Al metal matrix composites. Mater Sci Eng A 671:214–220. https://doi.org/10.1016/j.msea.2016.05.056

27. Khatami R, Fattah-alhosseini A, Keshavarz MK (2017) Effect of grain refinement on the passive and electrochemical behavior of 2024 Al alloy. J Alloys Compd 708:316–322. https://doi.org/10.1016/j.jallcom.2017.03.031

28. Li JF, Ziqiao Z, Na J, Chengyu T (2005) Localized corrosion mechanism of 2×××-series Al alloy containing S(Al$_2$CuMg) and θ′(Al$_2$Cu) precipitates in 4.0% NaCl solution at pH 6.1. Mater Chem Phys 91:325–329. https://doi.org/10.1016/j.matchemphys.2004.11.034

29. Guillaumin V, Mankowski G (1998) Localized corrosion of 2024 T351 aluminium alloy in chloride media. Corros Sci 41:421–438. https://doi.org/10.1016/S0010-938X(98)00116-4

30. Mahmoud TS (2008) Effect of friction stir processing on electrical conductivity and corrosion resistance of AA6063-T6 Al alloy. Proc Inst Mech Eng Part C J Mech Eng Sci 222:1117–1123. https://doi.org/10.1243/09544062JMES847

31. Flores JF, Neville A, Kapur N, Gnanavelu A (2012) Corrosion and erosion-corrosion processes of metal-matrix composites in slurry conditions. J Mater Eng Perform 21:395–405. https://doi.org/10.1007/s11665-011-9926-z

32. Ni DR, Xiao BL, Ma ZY et al (2010) Corrosion properties of friction-stir processed cast NiAl bronze. Corros Sci 52:1610–1617. https://doi.org/10.1016/j.corsci.2010.02.026

33. Narimani M, Lotfi B, Sadeghian Z (2015) Investigating the effect of tool dimension and rotational speed on microstructure of Al-B$_4$C surface composite layer produced by friction stir processing (FSP). J Adv Mater Process 3:61–70

34. Jalilvand MM, Mazaheri Y, Heidarpour A, Roknian M (2019) Development of A356/Al$_2$O$_3$+SiO$_2$ surface hybrid nanocomposite by friction stir processing. Surf Coatings Technol 360:121–132. https://doi.org/10.1016/j.surfcoat.2018.12.126

35. Navaser M, Atapour M (2017) Effect of friction stir processing on pitting corrosion and intergranular attack of 7075 aluminum alloy. J Mater Sci Technol 33:155–165. https://doi.org/10.1016/j.jmst.2016.07.008

36. Surekha K, Murty BS, Prasad Rao K (2009) Effect of processing parameters on the corrosion behaviour of friction stir processed AA2219 aluminum alloy. Solid State Sci 11:907–917. https://doi.org/10.1016/j.solidstatesciences.2008.11.007

37. Buchheit RG, Grant RP, Hlava PF et al (1997) Local dissolution phenomena associated with s phase (Al$_2$CuMg) particles in aluminum alloy 2024–T3. J Electrochem Soc 144:2621–2628. https://doi.org/10.1149/1.1837874

38. Liu Z, Chong PH, Skeldon P et al (2006) Fundamental understanding of the corrosion performance of laser-melted metallic alloys. Surf Coatings Technol 200:5514–5525. https://doi.org/10.1016/j.surfcoat.2005.07.108

39. Esmailzadeh S, Aliofkhazraei M, Sarlak H (2018) Interpretation of cyclic potentiodynamic polarization test results for study of corrosion behavior of metals: a review. Prot Met Phys Chem Surfaces 54:976–989. https://doi.org/10.1134/S207020511805026X

40. Argade GR, Panigrahi SK, Mishra RS (2012) Effects of grain size on the corrosion resistance of wrought magnesium alloys containing neodymium. Corros Sci 58:145–151. https://doi.org/10.1016/j.corsci.2012.01.021

41. Domínguez-Crespo MA, Torres-Huerta AM, Rodil SE et al (2010) XPS and EIS studies of sputtered Al-Ce films formed on AA6061 aluminum alloy in 3.5% NaCl solution. J Appl Electrochem 40:639–651. https://doi.org/10.1007/s10800-009-0039-4

42. Zhang Z, Liu F, Han EH, Xu L (2020) Mechanical and corrosion properties in 3.5% NaCl solution of cold sprayed Al-based coatings. Surf Coatings Technol 385:135539. https://doi.org/10.1016/j.surfcoat.2020.125372

43. Dong CF, Sheng H, An YH et al (2010) Corrosion of 7A04 aluminum alloy under defected epoxy coating studied by localized electrochemical impedance spectroscopy. Prog Org Coatings 67:269–273. https://doi.org/10.1016/j.porgcoat.2009.11.004

44. Burstein SH (2020) The chemistry, biology and pharmacology of the cyclopentenone prostaglandins. Prostaglandins Other Lipid Mediat 148:106408. https://doi.org/10.1016/j.prostaglandins.2020.106408

45. Liu J, Zhao K, Yu M, Li S (2018) Effect of surface abrasion on pitting corrosion of Al-Li alloy. Corros Sci 138:75–84. https://doi.org/10.1016/j.corsci.2018.04.010

46. Cao M, Liu L, Yu Z et al (2019) Electrochemical corrosion behavior of 2A02 Al alloy under an accelerated simulation marine atmospheric environment. J Mater Sci Technol 35:651–659. https://doi.org/10.1016/j.jmst.2018.09.060

47. Zhang W, Frankel GS (2003) Transitions between pitting and intergranular corrosion in AA2024. Electrochim Acta 48:1193–1210. https://doi.org/10.1016/S0013-4686(02)00828-9

48. Liu Y, Meng GZ, Cheng YF (2009) Electronic structure and pitting behavior of 3003 aluminum alloy passivated under various conditions. Electrochim Acta 54:4155–4163. https://doi.org/10.1016/j.electacta.2009.02.058